

# Electrons and phonons in pentacene, insights from comparison between experiment and simulations

Luca Gnoli<sup>1, \*</sup>, Elisabetta Venuti<sup>2</sup>, Raffaele Guido Della Valle<sup>2</sup>, Matteo Masino<sup>3</sup>, Patrizio Graziosi<sup>1</sup>,

<sup>1</sup> ISMN – CNR, Consiglio Nazionale delle Ricerche, via Gobetti 101, 40129, Bologna, Italy

<sup>2</sup> Dipartimento di Chimica Industriale "Toso Montanari", Università di Bologna, via Gobetti 85, 410129, Italy

<sup>3</sup> Dipartimento di Scienze Chimiche, Della Vita e Della Sostenibilità Ambientale & INSTM-UdR Parma, Parco Area delle Scienze, 17/A, 43124 Parma, Italy

\* [lucagnoli@cnr.it](mailto:lucagnoli@cnr.it)

## Abstract

We have computed the vibrational pattern and the electron-phonon coupling at several  $q$ -points in the Brillouin Zone for the three known pentacene polymorphs. After having verified that they effectively correspond to three different structures, we revisit the assignment of the experimental Raman modes. Finally, using a pool of post-processing tools, we present the phonon spectra and dispersions, confirming previous indications about the effect of phonon dispersion and charge mobility. In addition, we consider in an effective way the coexistence of more polymorphs and the possible role of defects and energy disorder.

## I. Introduction

Pentacene has been long time regarded as a benchmark Organic Semiconductors (OSCs); despite OSC field developed towards new functionalized system, pentacene still is an ideal standard to develop fundamental knowledge. [1–4] This is of special importance because, the widespread application of OSCs in electronics-related applications is hampered by the lack of predictive understanding of the inter-relationship between solid-state packing and performance of the device (whatever type of device). This challenge also arises from the existence of multiple crystal structures, known as polymorphism, for a given molecular compound. Each polymorph exhibits a distinct vibrational pattern, leading to variations in electron-phonon coupling (EPC), thereby influencing the transport characteristics of OSCs. [5,6] Indeed, low-frequency vibrational modes, such as translations and rotations of the entire molecule, play a pivotal role in introducing dynamic disorder which, in turn, affects the electronic transfer integrals and hence the bandwidth, ultimately shaping the macroscale electronic properties of the semiconductor. Therefore, understanding polymorphism is crucial for defining the electronic properties in OSCs at the macroscopic scale.

In this study, we first present accurate a validated first-principles calculations of the three known pentacene polymorphs: low temperature (LT), high temperature (HT) and thin film (TF). We use the inherent structures method [7–10] to ensure they are really three different structures, and assess their vibrational fingerprint. Then, we compute the EPC at the zone-boundary and demonstrate that the strongest EPC happens for modes having non-zero momentum, i.e. not in  $\Gamma$ . We can then perform the assignment of the experimental identified modes – a task still missing so far. Finally, we use the computed EPC to evaluate the mobility  $\mu$  [11] of the three polymorph and related mixture. [12] Also, we use pentacene as a benchmark to test the computational description of the role of disorder or defects in term of energy potential and carrier scattering.

## II. Computational method

### a. Electronic and Vibrational properties

We employ PBE pseudopotentials and the D3-BJ Grimme with Becke-Johnson damping functions for a posteriori VdW correction *at any stage* of a DFT calculation with VASP. [11,16–18] We start on the experimental unit cell parameters, optimize the k-points grid using a cutoff energy of 400 eV. After having detected a converging *k*-grid, respectively, we optimize the energy cutoff for the wavefunctions. Finally, we relax the atomic positions keeping constant the unit cell parameters at the experimental values. For the inherent structures study, we relax also the lattice parameters.

Following relaxation, Phonopy packages [19,20] are used to compute and diagonalize the dynamical matrix using a  $2 \times 2 \times 2$  super-cell – a setup validated to ensure convergence in phonon frequency and 3D density of states (DOS) without any negative frequency, except for the acoustic branches in  $\Gamma$ , for which negative frequency around  $10^{-1}$  -  $10^{-2}$  THz may be obtained and are considered acceptable. Finally, the off-resonant Raman activities were computed with the `vasp_Raman.py` program. [21] This program uses VASP as back-end to compute the polarizability with the approach of the finite displacements, and returns the Raman activity of the selected modes.

### b. Electron-phonon coupling (EPC)

We adopt a recently developed protocol to parametrize the EPC. [11] We modulate the unit cell along the selected eigenmodes for  $\Gamma$  point and all the relevant high-symmetry  $\mathbf{q}$ -points within the BZ, as given in the Bilbao crystallographic data center. [22,23] Thus, for each considered  $\mathbf{q}$  point and  $\nu$  phonon branch, a unit cell distorted along the eigenmode vibrational coordinate is generated. Phonopy code automatically weights for the atomic mass in this process. From the consideration that in the tight-binding approximation the dispersion energy can be approximated along a 1D direction to  $\sim 2 t_W \cos(\mathbf{k} \cdot \mathbf{a})$ , and that leads to a bandwidth  $B_W$  related to the transfer integral  $t_W$  by the relation  $B_W = 4t_W$ . [24] As a result, the comprehensive bandwidth across the full 3D Brillouin Zone, and hence the corresponding transfer integral, can be obtained from a first principle DFT electronic structure calculation.

Under this conceptual framework, and taking into account the traditional approach to EPC [25,26] and the conventional definition of Deformation Potentials, [27,28] the EPC constant for each  $\mathbf{q}$ -point and phonon branch  $\nu$  can be defined as: [11]

$$D_{\mathbf{q},\nu}^{n,n} = \frac{\partial t_W^n}{\partial \mathbf{r}_{\mathbf{q},\nu}} \quad (1)$$

$$D_{\mathbf{q},\nu}^{n,m} = \frac{\partial \Delta_s^{n,m}}{\partial \mathbf{r}_{\mathbf{q},\nu}} \quad (2)$$

In Eq. s (1)-(2),  $n$  and  $m$  are the band indexes,  $t_W^n$  is the bandwidth of the band of index  $n$ ,  $\Delta_s^{n,m}$  is the Davydov splitting between the bands  $n$  and  $m$ , computed as the energy difference between the energy barycenters of the bands,  $\mathbf{r}_{\mathbf{q},\nu}$  is the average displacements of all the atoms in the structure distorted along the eigenmode  $(\mathbf{q}, \nu)$ . Thus, Eq. (1) is related to *intra*-band processes, i.e. will be used when the carrier scattering involves initial and final states in the same band, while Eq. (2) is related to *inter*-band processes.

Operatively, after a self-consistent DFT calculation for each  $(\mathbf{q}, \nu)$  modulated/eigen-distorted structure, we perform a non-self-consistent calculation and save the obtained electronic structure in

.bxsf format [29] with the c2x code. [30] Ad hoc routines were developed to extract the EPC parameters as in Eq. s (1) and (2). Finally, since we will be considering states, and transitions, in the whole 3D electronic structure, a DOS-weighted average of the computed EPC, across the  $\mathbf{q}$ -points for each branch  $\nu$ , was performed to extract band-index specific EPC parameters to be used throughout the whole BZ:

$$D_{n,m,\nu} = \frac{\sum_{\mathbf{q}} D_{\mathbf{q},\nu}^{n,m^2} \text{DOS}_{\mathbf{q},\nu}}{\sum_{\mathbf{q}} \text{DOS}_{\mathbf{q},\nu}} \quad (3).$$

The selection of the vibrational modes to be considered in this protocol relies on the phonon DOS specifications and is made considering the modes which are bundled in the DOS. For pentacene, this encompasses the 20 modes of lowest frequency. The comprehensive EPC parametrized in Eq. (3) are regarded as the proper deformation potentials for inelastic processes involving non-polar phonons in the mobility calculation, as detailed in the next sub-section.

### c. Mobility

Crystalline OSCs exhibit a well-defined crystal structure, which manifests in a distinctive vibrational fingerprint. Adopting a description based on the electronic dispersions in the BZ of the reciprocal lattice the mobility  $\mu$  is evaluated from the conductivity  $\sigma$  as:

$$\mu_{ij(E_F,T)} = \frac{\sigma_{ij(E_F,T)}}{n \cdot q_0} \quad (4)$$

where  $i$  and  $j$  are the Cartesian components  $x$ ,  $y$ , and  $z$ , of the mobility and conductivity tensors,  $E_F$  is the Fermi level,  $T$  the temperature,  $n$  the carrier density and  $q_0$  the electronic charge. The conductivity is computed in the context of the linearized BTE as: [31]

$$\sigma_{ij(E_F,T)} = q_0^2 \int_E \Xi_{ij}(E) \left( -\frac{\partial f_0}{\partial E} \right) dE \quad (8)$$

The integrand of Eq. (8) contains the Transport Distribution Function (TDF)  $\Xi_{ij}$  and the energy derivative of the equilibrium Fermi-Dirac distribution  $f_0$ . The TDF is defined as:

$$\Xi_{ij}(E) = \frac{2}{(2\pi)^3} \sum_n \sum_{\mathbf{k}_{n,E}} v_{i,\mathbf{k}_{n,E}} v_{j,\mathbf{k}_{n,E}} \tau_{i,\mathbf{k}_{n,E}} g_{\mathbf{k}_{n,E}} \quad (9)$$

In Eq. (9)  $v$  is the band velocity,  $\tau$  the relaxation time, and  $g$  the electronic DOS. All these quantities are specific of each individual transport state  $\mathbf{k}_{n,E}$ , where  $\mathbf{k}$  is the wave-vector,  $n$  indicates the band index and  $E$  its energy. So, the sum runs over all the transport states identified by their momentum, belonging to all the bands, having a certain energy. The DOS  $g_{\mathbf{k}_{n,E}}$  is defined as  $\frac{dA_{\mathbf{k}_{n,E}}}{|\bar{v}_{\mathbf{k}_{n,E}}|}$ , where

$dA_{\mathbf{k}_{n,E}}$  represents the area of the surface element of the constant energy surface to which the  $\mathbf{k}_{n,E}$  state belongs, associated to each specific  $\mathbf{k}_{n,E}$  state. Therefore, the sum in Eq. 6 is performed for each constant energy surface to compute the energy dependent TDF which will be then integrated as in Eq. (8). In this work, the tetrahedron method has been employed to construct the constant energy surfaces and extract the related quantities. [32,33]

The relaxation time of the state  $\mathbf{k}_{n,E}$  for the transport along the direction  $i$ , related to scattering with a phonon belonging to the branch  $\nu$ , is evaluated from the inelastic scattering with non-polar phonons as (we omit the index  $\nu$  for clarity): [27,28,33–35]

$$\frac{1}{\tau_{i,\mathbf{k}_{n,E}}} = \frac{1}{(2\pi)^3} \sum_{\mathbf{k}'} \frac{\pi D_{n,n'}^2}{\rho \omega_0} \left( N_{\omega_0} + \frac{1}{2} \mp \frac{1}{2} \right) g_{\mathbf{k}',n',E'} \left( 1 - \frac{v_{i,\mathbf{k}',n',E'}}{v_{i,\mathbf{k}_{n,E}}} \right) \quad (10)$$

where  $D_{n,n'}$  is the deformation potential related to the electron-phonon scattering between the initial band  $n$  and the final band  $n'$ , which includes intra- and inter-band processes, evaluated from Eq. (1) or (2), respectively.  $\rho$  is the mass density,  $\omega_{0,\nu} = \frac{\sum_{\omega_\nu} \omega_\nu \cdot \text{DOS}(\omega_\nu)}{\sum_{\omega_\nu} \text{DOS}(\omega_\nu)}$  is the effective frequency for the branch  $\nu$  evaluated from a DOS-weighted average over the selected portion of the phonon spectrum,  $N_{\omega_0}$  represents the phonon Bose-Einstein statistical distribution,  $g_{\mathbf{k}',n',E'}$  is the DOS of the final state, belonging to the band  $n'$  and at energy  $E'$ , which is either increased or decreased by  $\hbar\omega$  for absorption or emission processes, respectively, denoted by “-” and “+” signs. The term  $\left( 1 - \frac{v_{i,\mathbf{k}',n',E'}}{v_{i,\mathbf{k}_{n,E}}} \right)$  approximates the momentum relaxation time, [34–36] which is the relevant type of relaxation time for computing transport coefficients. [28] Note that this definition of relaxation time bears similarity to what appears in other works on OSCs. [37] The calculation of the mobility is performed using the *ElectTra* simulator. [31,38]

Because the mobility tensor derived using equations is expressed in Cartesian coordinates, we project the electric field  $\vec{\mathcal{E}}$  along the crystallographic axes. This is achieved by inverting the lattice vector matrix, expressed in the POSCAR VASP file:

$$\vec{\mathcal{E}}_l = \mathbf{l} * \text{inv}(A) \quad (11)$$

where  $\mathbf{l}$  is the intended direction in the internal coordinates and  $A$  is the lattice vector matrix. This allows us to express the electric fields along the internal cell axes,  $\vec{\mathcal{E}}_a$ ,  $\vec{\mathcal{E}}_b$ , and  $\vec{\mathcal{E}}_c$  in Cartesian coordinates. Next, from the conductivity tensor  $\vec{\sigma}$ , given by Eq. (8), we compute a current density as:

$$\vec{J}_l = \vec{\sigma} \vec{\mathcal{E}}_l \quad (12).$$

Thus, we obtain a component of the conductivity tensor in internal coordinates:

$$\sigma_l = \frac{|\vec{J}_l|}{|\vec{\mathcal{E}}_l|} \quad (13)$$

and the related mobility:

$$\mu_l = \sigma_l / n \cdot q_0 \quad (14).$$

Using this approach, we can link the computed mobility tensor in Cartesian coordinates to the mobility measurable along specific crystal directions.

To perform the charge transport calculations, an additional non-self-consistent calculation on a finer mesh is needed. In this study, we adopted a  $28 \times 21 \times 11$ ,  $24 \times 18 \times 9$ , and  $28 \times 21 \times 11$ ,  $k$ -samplings, with cutoff energies of 800, 900, and 800 eV, for the LT, HT and TF polymorphs, respectively. Importantly, the energy resolution used to construct the constant energy surfaces is set at 1 meV, meaning that each surface is calculated every 1 meV for each band, from the band edge up to  $\sim 0.4$  eV. Such fine resolution proves to be essential for the treatment of the flatter bands of the OSC compared to inorganic compounds. [33, 39–41] Due to the large bandgap of pentacene, we perform unipolar calculations separately for electron mobility in the conduction band (CB) and hole mobility in the valence band (VB).

### III. Results and Discussion

#### a. Inherent Structures

Starting from the structures in the CCDC database, from which we took HT [42], LT [42], and TF [43] cif files, we first relax the atomic positions. The results are reported in Table 1. We clearly see that at the experimental lattice parameters of the polymorphs, the ranking in energy is driven by the dispersive VdW contribution. This states the relevance of the VdW contribution in stabilizing experimental observed structures. Then, we conduct an inherent structures study by relaxing the cell parameters, i.e. assuming  $T = 0$  K, with the purpose of observing if some minima coincide. The final energies, reported in Table 2, show that three structures have actually different energies and are three different polymorphs. Moreover, the energy ranking is not driven by a single contribution but both electronic and dispersive contribution are relevant to detect the ranking. Interestingly, the TF polymorph, similar to the HT on spectroscopy ground, [12] is closer in energy to the LT polymorph. The different characters of the three polymorphs can be observed also in the Raman spectra, shown in Figure 1a and in section III.b.

Table 1: total ( $E_{\text{tot}}$ ), electronic ( $E_{\text{electr}}$ ) and VdW ( $E_{\text{disp}}$ ) energies, in eV, after relaxation of the atomic position at fixed cell.

Atomic relax.	$E_{\text{tot}}$	$E_{\text{electr}}$	$E_{\text{disp}}$
HT	-505.95925377	-499.89884901	-6.06040
TF	-506.01845836	-499.79581002	-6.22265
LT	-506.04048098	-499.70372775	-6.33675

Table 2: total ( $E_{\text{tot}}$ ), electronic ( $E_{\text{electr}}$ ) and VdW ( $E_{\text{disp}}$ ) energies, in eV, after unit cell relaxation.

u.c. relax.	$E_{\text{tot}}$	$E_{\text{electr}}$	$E_{\text{disp}}$
HT	-506.05713354	-499.47794422	-6.57919
TF	-506.06523307	-499.52382943	-6.54140
LT	-506.06800958	-499.46723052	-6.60078

### b. Vibrational properties

The vibrational properties were computed for the three polymorphs. We first show the Raman spectra of the three polymorphs for the completely relaxed structure obtained in the inherent structures study, in Fig. 1a. It is clear that the Raman pattern is different; when the structures are left completely free to relax in their energy minimum, they achieve different energy minima, with diverse vibrational structure. The inset in Fig. 1a highlights the lowest frequency region, confirming the different pattern.

The Raman spectra measured for the experimental structure, adjusted for laser frequency and temperature, [11,44] are displayed in Fig. 1b. We confirm the typical structure of two triplets, [12] well grouped for HT and LT and a bit more sparse for the TF. The decomposition in inter-molecular motions show that the first triplet is mostly intermolecular and consisting of rotations around the median and normal molecular axes. Differently, in the second triplet, the lowest two modes are nearly completely intermolecular in nature, being rotation around the long molecule axis, while the highest energy mode is mostly internal, especially in HT and TF.

The spectra are drawn as Lorentzian bands with a FWHM of 1/3 of the mean distance between the frequencies, chosen to conform to the experimental features of P1. The positions of the peaks

agree within a few  $\text{cm}^{-1}$ , less than 5, reported also in the Supplemental Material, [45] thus confirming the validity of our description in terms of pseudopotentials and electronic structure. [16,18,46,47] The experimental relative intensity maps satisfactorily agree with the simulated ones once the laser excitation frequency and the measurement temperature of the experiments are accounted for. [44] This is obtained with the formula  $I = I_0 \frac{\nu}{(\nu - \nu_0)^4} \left(1 - \exp\left(\frac{-h\nu}{kT_0}\right)\right)$ , where  $I_0$ ,  $\nu_0$ ,  $T_0$ , and  $\nu$  are the measured intensity, excitation frequency, temperature and vibration frequency, respectively,  $h$  is the Planck constant and  $k$  the Boltzmann constant..  $I$  is the adjusted experimental intensity.

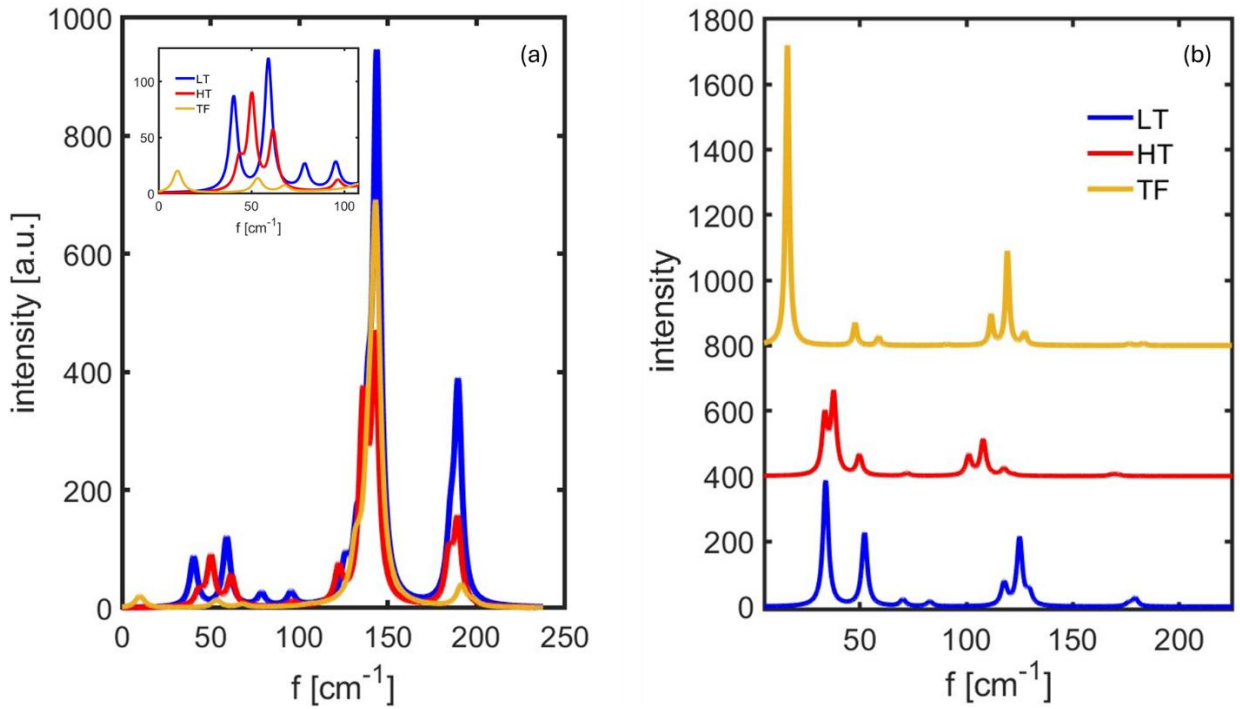


Figure 1: Raman spectra for the completely relaxed structures (a) and experimentally measured unit cells (b). In (b), the reported intensity is adjusted for the laser frequency and measurement temperature.

We show the comparison between computed and experimental frequency in Table 3. Moreover, for the HT polymorph, we used two structures, the one by Campbell [48] and the one by Siegrist [42]. The assignment of the symmetry is performed using the `simmetry.py` software, a post-processing routine which exploits the projectors method [49]. We briefly recall here that only  $A_g$  modes are visible in Raman experiments, and that in  $P_{\bar{1}}$  symmetry, the intermolecular vibrational character of the eigenmodes is rotational for  $A_g$  modes and translational for  $A_u$  modes. Also, we used the experimental cells; thus, a softening in respect of the low temperature frequency is expected. The present study allows finally the assessment of the nature of the modes observed in Raman experiments.



Table 3: experimental Raman frequency for HT [50], LT [50], and TF [12], compared with the computed values. We stress that when computing the Raman frequency we keep the experimental lattice constant, thus a softening is expected for structures measured at high temperature.

Experimental Polym. C (Campbell)		Computed HT 478 K (Siegrist)	Computed HT 295 K (Campbell)	Experimental Polym. H (Holmes)		Computed LT	Exp. TF 300 K	Computed TF
80 K	300 K			80 K	300 K			
		25.6 (Au)	28.7 (Au)	44.9	37.6	33.9 (Ag)		16.0 (Ag)
49.4	41.5	33.5 (Ag)	35.4 (Ag)			36.8 (Au)		36.0 (Au)
54.9	49.9	37.7 (Ag)	42.6 (Ag)	65.5	56.2	52.2 (Ag)	~ 50	47.7 (Ag)
		49.6 (Au)	52.9 (Au)			54.0 (Au)		48.0 (Au)
66.9	60.5	49.7 (Ag)	54.6 (Ag)			66.2 (Au)		80.9 (Au)
		58.3 (Au)	64.9 (Au)	84.3	74.8	70.2 (Ag)		90.8 (Ag)
		72.1 (Ag)	82.2 (Ag)	99.1	92.0	82.8 (Ag)		92.3 (Au)
		78.1 (Au)	87.6 (Au)			85.4 (Au)		111.6 (Ag)
		82.2 (Au)	94.13 (Au)			95.6 (Au)		119.3 (Ag)
99.8	94.4	101.1 (Ag)	112.0 (Ag)	132.2	128	117.1 (Ag)		120.4 (Au)
126.7	119.5	107.9 (Ag)	121.5 (Ag)	136.2	133	118.0 (Ag)		124.6 (Au)
		114.0 (Au)	122.1 (Au)			121.0 (Au)		126.8 (Ag)
140.6	136.6	117.7 (Ag)	124.6 (Au)			122.6 (Au)	~ 135	127.5 (Ag)
		119.2 (Au)	126.2 (Ag)			124.7 (Au)		134.8 (Au)
		121.9 (Ag)	127.1 (Au)	144.1	149.5	124.9 (Ag)		137.1 (Au)
		123.0 (Au)	128.3 (Ag)			129.6 (Ag)		176.6(Ag)
		128.3 (Au)	137.6 (Au)			135.9 (Au)		183.0 (Ag)
147.5		168.5 (Ag)	175.8 (Ag)	191.3		176.2 (Ag)		187.3 (Au)
		171.2 (Ag)	179.0 (Ag)	196.8		179.3 (Ag)		198.5 (Au)

The phonon dispersions and the corresponding DOS are reported in Figure 2. The dispersions along directions connecting high symmetry  $\mathbf{q}$ -points are shown in Figures 2a-c. It is important to note that the first 20 modes are bundled together throughout the BZ. This feature is highlighted in Figure 2d, where the DOS of the polymorphs are reported. Thus, we consider them as 20 scattering channels, following the common approach in semiconductors, [28] and due to the dispersion through the BZ, we assign to each of them an effective phonon frequency  $\omega_{0,\nu}$  [11]. Because of their bundled character, we consider all of them and cut our region of interest at the first drop to zero of the phonon DOS.

On the grounds of previous indications [12], we highlight the dispersions of the Raman active modes for the three polymorphs along the  $c$  axis in Fig. 2e. The TF polymorph features slightly less dispersed modes along  $c$  axis direction, above  $50 \text{ cm}^{-1}$ , which is also the growth direction. Thus, a certain disorder along the growth direction might cause the modes to be more difficult to be detected. However, we cannot rule out the possibility that the reduced number of layers in the film causes the break of the theoretical periodicity, preventing the identification of the modes in  $\Gamma$ .

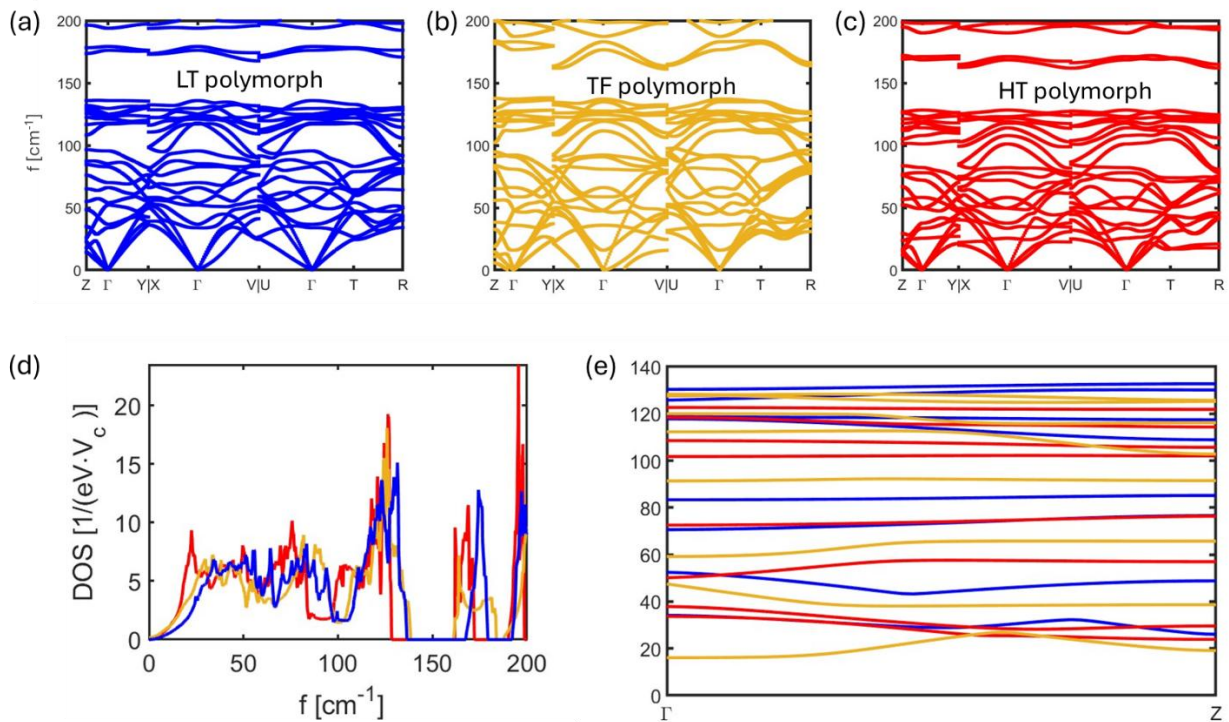


Figure 2: phonons dispersions for the three polymorphs (a-c) and their DOS (d). In (e) we compare the dispersions of the Raman active modes of the three polymorphs, along the  $c$  axis.

### c. EPC parameters

In this section, we present the EPCs evaluation according to Eq. s (1)-(3). They have been computed with Phonopy for unit cells with atoms displaced along each eigenmode, after convergence tests showing 0.0025 Å as displacement value. In Table 4, we report the mode,  $q$ -point pair for which the EPC is above 85 % of the highest value. We first note that no modes are in  $\Gamma$ . This demonstrates the importance of not confining the analysis to the BZ center [51] even if the spectroscopically achievable modes belong to  $\Gamma$ . Also, we notice that the HT has four modes with strong EPC while the LT has only two modes, with EPC comparable to the HT, while the TF has two modes with stronger EPC than the other polymorphs. In Table 4, we also report the effective EPC for that mode and  $q$ -point, evaluated as the EPC squared divided by the phonon energy, after eq. (10). We see that the effective scattering strength in the LT drops while in the other polymorphs stays high; as we see in section III.d, this influences the mobility.

Table 4: EPC values in eV/Å for tetracene PF, comprising the lowest 16 modes at 8 high symmetry  $q$ -points in the BZ, as indicated. (a) and (b), EPC computed with Eq. (1) for the two CBs, (c) EPC computed from the Davydov splitting as in Eq. (2). (d)-(f), same as (a)-(c) for the VBs.

Polymorph	$q$ -point	Freq. cm <sup>-1</sup>	EPC eV/Å	EPC <sup>2</sup> /ħω [eV/√Å]	symm.	T <sub>L</sub>	T <sub>M</sub>	T <sub>N</sub>	R <sub>L</sub>	R <sub>M</sub>	R <sub>N</sub>
HT	V	45.3	0.35	21.8	A	5	34	8	5	2	10
HT	R	41.6	0.33	21.1	A	0	3	1	1	14	20
HT	X	46.9	0.30	15.5	A	0	44	9	12	0	10
HT	U	49.9	0.30	14.5	A	0	31	1	6	4	20
TF	V	47.9	0.49	40.4	A	1	2	1	3	4	67
TF	U	45.7	0.43	32.6	A	4	26	1	2	1	16
LT	U	26.7	0.27	22.0	A	67	0	1	1	0	3
LT	X	39.2	0.24	11.9	A	46	2	1	0	2	4

#### d. Mobility

In this section, we summarize the results achieved in terms of transport properties. First, we observe that the phonon-limited study reproduces the experimental rank. We use the approach in eq.s (11) to (14) to obtain the mobility projected along arbitrary 3D orientations and compute an average mobility  $\mu_t$  using more than  $10^6$  random orientations. For the LT, HT and TF, at room temperature, we find  $\mu_t = 28.8, 6.5, \text{ and } 5.7 \text{ cm}^2/\text{Vs}$ , respectively. To enforce our comparison with experimental results, in Table 5, we compare the computed mobilities with the experimental values of the best-case scenarios we found in literature for bulk single-crystal (s.c.) [52], single-crystal field effect transistor (s.c.-FET) [53], and thin film field effect transistor (TF-FET) [54]. The calculated mobility is along  $b$  axis,  $\mu_b$ , in the  $ab$  plane,  $\mu_{\langle ab \rangle}$ , and also averaged over two million of random orientations,  $\mu_t$ .

In Table 5, for the TF-FET case, we report also the case of a mixture of two polymorphs, where the mixture is treated as inhomogeneous two-components medium [55], leading to:

$$\mu = \mu_1^{f_1} \mu_2^{1-f_1} \quad (15),$$

Where 1 and 2 are the two phases and  $f_1$  is the volume fraction of the first phase. In our estimates in Table 5, we assumed that TF and HT coexist [12] in equal amount. Also, the different islands can have different structures at the coalescence boundary. Thus, we phenomenologically introduce a scattering term with characteristic energy equal to the energy distance between the top-valence band and other satellite valleys at lower energy in the HT phase,  $\Delta E_V^{\text{HT}}$ , which is 32.5 meV. We consider only HT since TF appears not to have such satellite valleys but only a valence band maximum without relative maxima. We treat such boundary scattering on the foot of the Fermi golden rule, using such characteristic energy as scattering potential  $U_b$  and the energy dependent density of the states of the unit cell  $g_{uc(E)}$ . Thus, we have a scattering time  $\tau_{b(E)}$  for this boundary scattering:

$$\frac{1}{\tau_{b(E)}} = \frac{2\pi}{\hbar} (U_b)^2 g_{uc(E)} \quad (16).$$

We used eq. (16) also to account, in a macroscopic and phenomenological way, of structural defects in single crystals, where an effective barrier of  $\sim 40$  meV brings the phonon mobility in the measured range. Lastly, after the Kelvin probe microscopy (KPM) measurements on in operando pentacene FET, which revealed a  $\sim 0.1$  V voltage drop at any coalescence boundary between islands, [3] we used eq. (16) with  $U_b = 0.1$  eV, together with a 1:1 polymorph mixture. The obtained  $\mu$  is lower than the value measured in FET with polymeric gate [54], but is closer to what measured in the same experiment of KPM measurements [3], which featured oxide gate dielectrics. Thus, our preliminary results suggest that the strong impact of the dielectric/OSC interface [56] occurs also at the level of crystal quality and defectivity of the OSC.

Table 5: comparison between experimental and calculated  $\mu$  values, the crystal direction is at subscript and considered polymorph phase is in parenthesis. When eq. (16) is included, it is indicated. The asterisk indicates a mixture treated as from eq. (15).

System	Experimental $\mu$ [ $\text{cm}^2/\text{Vs}$ ]	Calculated $\mu$ [ $\text{cm}^2/\text{Vs}$ ]
s.c.	35 <sup>[52]</sup>	$\mu_b = 52$ (LT)
s.c. - FET	5.7 <sup>[53]</sup>	$\mu_{\langle ab \rangle} = 36$ (LT) 5.9 (LT, $U_b = 40$ meV)
TF-FET	3 <sup>[54]</sup>	$\mu_{\langle ab \rangle} = 7.1$ (TF) $\mu_r = 5.7$ (TF) $\mu_{\langle ab \rangle}^* = 4.2$ (TF:HT=1:1, $U_b = \Delta E_V^{\text{HT}} = 32.5$ meV) $\mu_{\langle ab \rangle}^* = 1.6$ (TF:HT=1:1, $U_b = 0.1$ eV)

#### IV. Conclusions

We used a solid first-principles method to shed light on the polymorphic nature of pentacene. After the demonstration of the genuine nature of the polymorphs, we performed the assignment of the experimental Raman modes and computed the EPC, finding that the EPC is extremely sensitive to little variation in the packing structure. In addition, we evaluated the mobility of the three polymorphs and compared with experimental results, reproducing the experimental ranking. Finally, we applied a phenomenological model to account, in a macroscopic way, microscopical disorder effect, which moves the values towards quantitative agreement.

#### Acknowledgement

We are thankful to prof. Alberto Girlando for fruitful discussions. We acknowledge the CINECA award under the ISCRA initiative, for the availability of high-performance computing resources and support. We acknowledge funding from the European Union–Next-Generation EU via the Italian call PRIN 2022, project code 2022XZ2ZM8, “POLYPHON”. T.S. thanks the Programma per Giovani Ricercatori “Rita Levi Montalcini” year 2020 (grant PGR20QN52R) of the Italian Ministry of University and Research (MUR) for the financial support. We acknowledge funding for the VASP license from the company M.M.B. s.r.l., Faenza (RA) Italy.

## References

- [1] A. Landi, A. Troisi, and A. Peluso, Explaining different experimental hole mobilities: influence of polymorphism on dynamic disorder in pentacene, *J. Mater. Chem. C* **7**, 9665 (2019).
- [2] X. Xie and A. Troisi, Evaluating the Electronic Structure of Coexisting Excitonic and Multiexcitonic States in Periodic Systems: Significance for Singlet Fission, *J. Chem. Theory Comput.* **18**, 394 (2022).
- [3] P. Annibale, C. Albonetti, P. Stoliar, and F. Biscarini, High-Resolution Mapping of the Electrostatic Potential in Organic Thin-Film Transistors by Phase Electrostatic Force Microscopy, *J. Phys. Chem. A* **111**, 12854 (2007).
- [4] S. Drakopoulou et al., Nanoscale Quantized Oscillations in Thin-Film Growth Greatly Enhance Transconductance in Organic Transistors, *Advanced Electronic Materials* **9**, 2300320 (2023).
- [5] S. Fratini, M. Nikolka, A. Salleo, G. Schweicher, and H. Sirringhaus, Charge transport in high-mobility conjugated polymers and molecular semiconductors, *Nat. Mater.* **19**, 491 (2020).
- [6] G. Schweicher et al., Chasing the “Killer” Phonon Mode for the Rational Design of Low-Disorder, High-Mobility Molecular Semiconductors, *Advanced Materials* **31**, 1902407 (2019).
- [7] R. G. Della Valle, E. Venuti, A. Brillante, and A. Girlando, Inherent Structures of Crystalline Tetracene, *J. Phys. Chem. A* **110**, 10858 (2006).
- [8] R. G. Della Valle, E. Venuti, A. Brillante, and A. Girlando, Inherent structures of crystalline pentacene, *The Journal of Chemical Physics* **118**, 807 (2003).
- [9] R. G. Della Valle, A. Brillante, E. Venuti, L. Farina, A. Girlando, and M. Masino, Exploring the polymorphism of crystalline pentacene, *Organic Electronics* **5**, 1 (2004).
- [10] E. Venuti, R. G. Della Valle, A. Brillante, M. Masino, and A. Girlando, Probing Pentacene Polymorphs by Lattice Dynamics Calculations, *J. Am. Chem. Soc.* **124**, 2128 (2002).
- [11] P. Graziosi, R. G. Della Valle, T. Salzillo, S. D’Agostino, M. Zangari, E. Cané, M. Masino, and E. Venuti, Electron-phonon coupling and mobility modeling in organic semiconductors: Method and application to two tetracene polymorphs, *Phys. Rev. Mater.* **9**, 024603 (2025).
- [12] A. Brillante et al., Structure and dynamics of pentacene on SiO<sub>2</sub>: From monolayer to bulk structure, *Phys. Rev. B* **85**, 195308 (2012).
- [13] Ö. H. Omar, M. del Cueto, T. Nematiram, and A. Troisi, High-throughput virtual screening for organic electronics: a comparative study of alternative strategies, *J. Mater. Chem. C* **9**, 13557 (2021).
- [14] J. M. Ha, S. H. Hur, A. Pathak, J.-E. Jeong, and H. Y. Woo, Recent advances in organic luminescent materials with narrowband emission, *NPG Asia Mater* **13**, 1 (2021).
- [15] J. Ma et al., The 2021 battery technology roadmap, *J. Phys. D: Appl. Phys.* **54**, 183001 (2021).
- [16] N. Bedoya-Martínez et al., DFT-Assisted Polymorph Identification from Lattice Raman Fingerprinting, *J. Phys. Chem. Lett.* **8**, 3690 (2017).
- [17] A. Giunchi, L. Pandolfi, R. G. Della Valle, T. Salzillo, E. Venuti, and A. Girlando, Lattice Dynamics of Quinacridone Polymorphs: A Combined Raman and Computational Approach, *Crystal Growth & Design* **23**, 6765 (2023).
- [18] T. Kamencek, S. Wieser, H. Kojima, N. Bedoya-Martínez, J. P. Dürholt, R. Schmid, and E. Zojer, Evaluating Computational Shortcuts in Supercell-Based Phonon Calculations of Molecular Crystals: The Instructive Case of Naphthalene, *J. Chem. Theory Comput.* **16**, 2716 (2020).
- [19] A. Togo, First-principles Phonon Calculations with Phonopy and Phono3py, *J. Phys. Soc. Jpn.* **92**, 012001 (2023).
- [20] A. Togo, L. Chaput, T. Tadano, and I. Tanaka, Implementation strategies in phonopy and phono3py, *J. Phys.: Condens. Matter* **35**, 353001 (2023).
- [21] raman-sc/VASP, (2024).

- [22] M. I. Aroyo, D. Orobengoa, G. de la Flor, E. S. Tasci, J. M. Perez-Mato, and H. Wondratschek, Brillouin-zone database on the Bilbao Crystallographic Server, *Acta Crystallographica Section A* **70**, 126 (2014).
- [23] An introduction to the tools hosted in the Bilbao Crystallographic Server | EPJ Web of Conferences, (n.d.).
- [24] C. Winkler, F. Mayer, and E. Zojer, Analyzing the Electronic Coupling in Molecular Crystals—The Instructive Case of  $\alpha$ -Quinacridone, *Advanced Theory and Simulations* **2**, 1800204 (2019).
- [25] A. Girlando, L. Grisanti, M. Masino, I. Bilotti, A. Brillante, R. G. Della Valle, and E. Venuti, Peierls and Holstein carrier-phonon coupling in crystalline rubrene, *Phys. Rev. B* **82**, 035208 (2010).
- [26] M. Masino, T. Salzillo, A. Brillante, R. G. Della Valle, E. Venuti, and A. Girlando, Experimental Estimate of the Holstein Electron–Phonon Coupling Constants in Perylene, *Advanced Electronic Materials* **6**, 2000208 (2020).
- [27] B. R. Nag, *Electron Transport in Compound Semiconductors* | SpringerLink (n.d.).
- [28] M. Lundstrom, *Fundamentals of Carrier Transport*, 2nd ed. (Cambridge University Press, Cambridge, 2000).
- [29] A. Kokalj, XCrySDen—a new program for displaying crystalline structures and electron densities, *Journal of Molecular Graphics and Modelling* **17**, 176 (1999).
- [30] M. J. Rutter, C2x: A tool for visualisation and input preparation for Castep and other electronic structure codes, *Computer Physics Communications* **225**, 174 (2018).
- [31] P. Graziosi, Z. Li, and N. Neophytou, *ElecTra* code: Full-band electronic transport properties of materials, *Computer Physics Communications* **287**, 108670 (2023).
- [32] G. Lehmann and M. Taut, On the Numerical Calculation of the Density of States and Related Properties, *Physica Status Solidi (b)* **54**, 469 (1972).
- [33] P. Graziosi, C. Kumarasinghe, and N. Neophytou, Impact of the scattering physics on the power factor of complex thermoelectric materials, *Journal of Applied Physics* **126**, 155701 (2019).
- [34] N. Neophytou and H. Kosina, Effects of confinement and orientation on the thermoelectric power factor of silicon nanowires, *Phys. Rev. B* **83**, 245305 (2011).
- [35] N. Neophytou and H. Kosina, Atomistic simulations of low-field mobility in Si nanowires: Influence of confinement and orientation, *Phys. Rev. B* **84**, 085313 (2011).
- [36] M. V. Fischetti and S. E. Laux, Band structure, deformation potentials, and carrier mobility in strained Si, Ge, and SiGe alloys, *Journal of Applied Physics* **80**, 2234 (1996).
- [37] S. Fratini and S. Ciuchi, Dynamical localization corrections to band transport, *Phys. Rev. Res.* **2**, 013001 (2020).
- [38] P. Graziosi, PatrizioGraziosi/ELECTRA, (2024).
- [39] P. Graziosi, C. Kumarasinghe, and N. Neophytou, Material Descriptors for the Discovery of Efficient Thermoelectrics, *ACS Appl. Energy Mater.* **3**, 5913 (2020).
- [40] Z. Li, P. Graziosi, and N. Neophytou, Deformation potential extraction and computationally efficient mobility calculations in silicon from first principles, *Phys. Rev. B* **104**, 195201 (2021).
- [41] Z. Li, P. Graziosi, and N. Neophytou, Efficient first-principles electronic transport approach to complex band structure materials: the case of n-type Mg<sub>3</sub>Sb<sub>2</sub>, *Npj Comput Mater* **10**, 1 (2024).
- [42] *Enhanced Physical Properties in a Pentacene Polymorph - Siegrist - 2001 - Angewandte Chemie International Edition - Wiley Online Library*, [https://onlinelibrary.wiley.com/doi/10.1002/1521-3773\(20010504\)40:9%3C1732::AID-ANIE17320%3E3.0.CO;2-7](https://onlinelibrary.wiley.com/doi/10.1002/1521-3773(20010504)40:9%3C1732::AID-ANIE17320%3E3.0.CO;2-7).
- [43] S. Schiefer, M. Huth, A. Dobrineski, and B. Nickel, Determination of the Crystal Structure of Substrate-Induced Pentacene Polymorphs in Fiber Structured Thin Films, *J. Am. Chem. Soc.* **129**, 10316 (2007).
- [44] D. Michalska and R. Wysockiński, The prediction of Raman spectra of platinum(II) anticancer drugs by density functional theory, *Chemical Physics Letters* **403**, 211 (2005).
- [45] See Supplemental Material at, (n.d.).

- [46] T. Salzillo, S. d'Agostino, A. Rivalta, A. Giunchi, A. Brillante, R. G. Della Valle, N. Bedoya-Martínez, E. Zojer, F. Grepioni, and E. Venuti, Structural, Spectroscopic, and Computational Characterization of the Concomitant Polymorphs of the Natural Semiconductor Indigo, *J. Phys. Chem. C* **122**, 18422 (2018).
- [47] T. Salzillo, A. Giunchi, M. Masino, N. Bedoya-Martínez, R. G. Della Valle, A. Brillante, A. Girlando, and E. Venuti, An Alternative Strategy to Polymorph Recognition at Work: The Emblematic Case of Coronene, *Crystal Growth & Design* **18**, 4869 (2018).
- [48] R. B. Campbell, J. M. Robertson, and J. Trotter, The crystal structure of hexacene, and a revision of the crystallographic data for tetracene, *Acta Cryst* **15**, 289 (1962).
- [49] R. G. Della Valle, L. Halonen, and E. Venuti, Molecular anharmonicity: A computer-aided treatment, *Journal of Computational Chemistry* **20**, 1716 (1999).
- [50] R. G. Della Valle, E. Venuti, L. Farina, A. Brillante, M. Masino, and A. Girlando, Intramolecular and Low-Frequency Intermolecular Vibrations of Pentacene Polymorphs as a Function of Temperature, *J. Phys. Chem. B* **108**, 1822 (2004).
- [51] D. Vong et al., Quantitative Hole Mobility Simulation and Validation in Substituted Acenes, *J. Phys. Chem. Lett.* **13**, 5530 (2022).
- [52] O. D. Jurchescu, J. Baas, and T. T. M. Palstra, Effect of impurities on the mobility of single crystal pentacene, *Applied Physics Letters* **84**, 3061 (2004).
- [53] J. Dong, P. Yu, S. A. Arabi, J. Wang, J. He, and C. Jiang, Enhanced mobility in organic field-effect transistors due to semiconductor/dielectric interface control and very thin single crystal, *Nanotechnology* **27**, 275202 (2016).
- [54] H. Klauk, M. Halik, U. Zschieschang, G. Schmid, W. Radlik, and W. Weber, High-mobility polymer gate dielectric pentacene thin film transistors, *Journal of Applied Physics* **92**, 5259 (2002).
- [55] V. V. Kabanov, K. Zagar, and D. Mihailovic, Electric conductivity of inhomogeneous two-component media in two dimensions, *J. Exp. Theor. Phys.* **100**, 715 (2005).
- [56] A. F. Stassen, R. W. I. de Boer, N. N. Iosad, and A. F. Morpurgo, Influence of the gate dielectric on the mobility of rubrene single-crystal field-effect transistors, *Applied Physics Letters* **85**, 3899 (2004).